Nanoscale Horizons



COMMUNICATION

View Article Online



Cite this: Nanoscale Horiz., 2025, **10**, 2381

Received 26th February 2025, Accepted 9th July 2025

DOI: 10.1039/d5nh00110b

rsc.li/nanoscale-horizons

Biomimetic nanozymes catalyze cascade reactions for enhanced tumor nanocatalytic therapy?

Cong-Min Huo, (1) ‡a Peng-Li Ding, ‡a Si-Ye Tong, ‡a Houjuan Zhu, (10) Shuo Gao. Yun-Yi Li,^c Jing-Yi Zhu 🕩 *and Wei Xue

Nano-catalytic therapy is an emerging tumor therapeutic strategy that has received considerable attention in recent years. This approach can convert endogenous hydrogen peroxide (H2O2) at the tumor site into highly toxic hydroxyl radicals (*OH) via a Fenton or Fenton-like reaction catalyzed by metal ions. However, the low levels of *OH generated merely from endogenous H2O2 are usually insufficient to effectively kill cancer cells. To address this limitation, we developed an efficient biomimetic nanozyme (HMPB/LAP@TK-CCM) designed to amplify intracellular oxidative stress and alleviate tumor hypoxia for enhanced nano-catalytic therapy. This nanozyme is loaded with the anticancer drug β-lapachone (LAP), which increases H₂O₂ levels within the tumor cells, thus enhancing the Fenton reaction of HMPB. The camouflaging strategy using a cancer-thylakoid hybrid membrane reduces the immune clearance of the nanoparticles and promotes their accumulation at the tumor site. The thylakoid membrane (TK) also contains natural catalase, which alleviates tumor hypoxia by producing oxygen, thus facilitating the generation of H2O2 by LAP and further enhancing the synergistic anti-tumor effect. Furthermore, in vivo studies demonstrated that HMPB/LAP@TK-CCM NPs effectively restrain tumor progression without negatively impacting normal tissues.

Introduction

Nanocatalytic therapy is an emerging and promising cancer treatment that eradicates tumor cells by converting intracellular

New concepts

This study introduces a novel nanozyme, a hybrid membrane-camouflaged hollow mesoporous Prussian blue (HMPB) nanocatalyst system loaded with the anticancer drug β-lapachone (LAP), designed to amplify intracellular oxidative stress and alleviate tumor hypoxia for enhanced nano-catalytic therapy. The key innovation lies in the combination of LAP, which elevates intracellular H2O2 levels, with HMPB nanoparticles, thus enhancing their Fenton reaction capabilities and strong photothermal properties. Moreover, the integration of a hybrid membrane composed of cancer cell membranes and spinach-derived thylakoid membranes further optimizes targeted delivery while alleviating tumor hypoxia. Unlike traditional approaches that rely solely on external H2O2 supplementation or enzyme delivery, this system effectively uses the tumor's intrinsic biology to catalyze and sustain the Fenton-like reaction in a selfamplifying manner. This innovative strategy offers enhanced therapeutic efficacy with minimized off-target effects, providing new insights into nanocatalytic cancer therapies and opening avenues for more efficient, tumor-selective treatments in clinical settings.

hydrogen peroxide (H2O2) into hydroxyl radicals (OH) through a transition metal nanoparticle (NP)-catalyzed reaction, known as the Fenton reaction. 1-3 The efficiency of this reaction and effective delivery of the catalytic nanozyme are crucial for successful cancer nano-catalytic therapy. 4,5 An efficient Fenton reaction requires an adequate iron source and a high concentration of H₂O₂. Targeted delivery of nanozymes can provide an adequate iron source.7 In fact, intracellular H2O2 levels in cancer cells are often insufficient, preventing Fenton agents from producing enough OH to effectively induce apoptosis.8,9 To elevate the intracellular H2O2 concentration, researchers have utilized natural glucose oxidase to convert endogenous glucose into gluconic acid and H₂O₂. 10,11 However, the low stability and high cost of glucose oxidase pose significant challenges for its practical use. 12,13 Thus, there is an urgent need to develop a simple and effective strategy to increase intracellular hydrogen peroxide concentration.

As reported, β-lapachone (LAP), a potent anticancer agent, catalyzes the production of H2O2 via NADPH-quinone oxidoreductase 1 (NQO1), an enzyme that is overexpressed in many

^a Key Laboratory of Biomaterials of Guangdong Higher Education Institutes, Guangdong Provincial Engineering and Technological Research Center for Drug Carrier Development, Department of Biomedical Engineering, Jinan University, Guangzhou, 510632, China. E-mail: jyzhu@jnu.edu.cn, weixue_jnu@aliyun.com

^b Institute of Materials Research and Engineering, Agency for Science, Technology and Research (A*STAR), 2 Fusionopolis Way, 138634, Singapore

^c Department of Nephrology, First Affiliated Hospital of Jinan University, Guangzhou, 510630, P. R. China

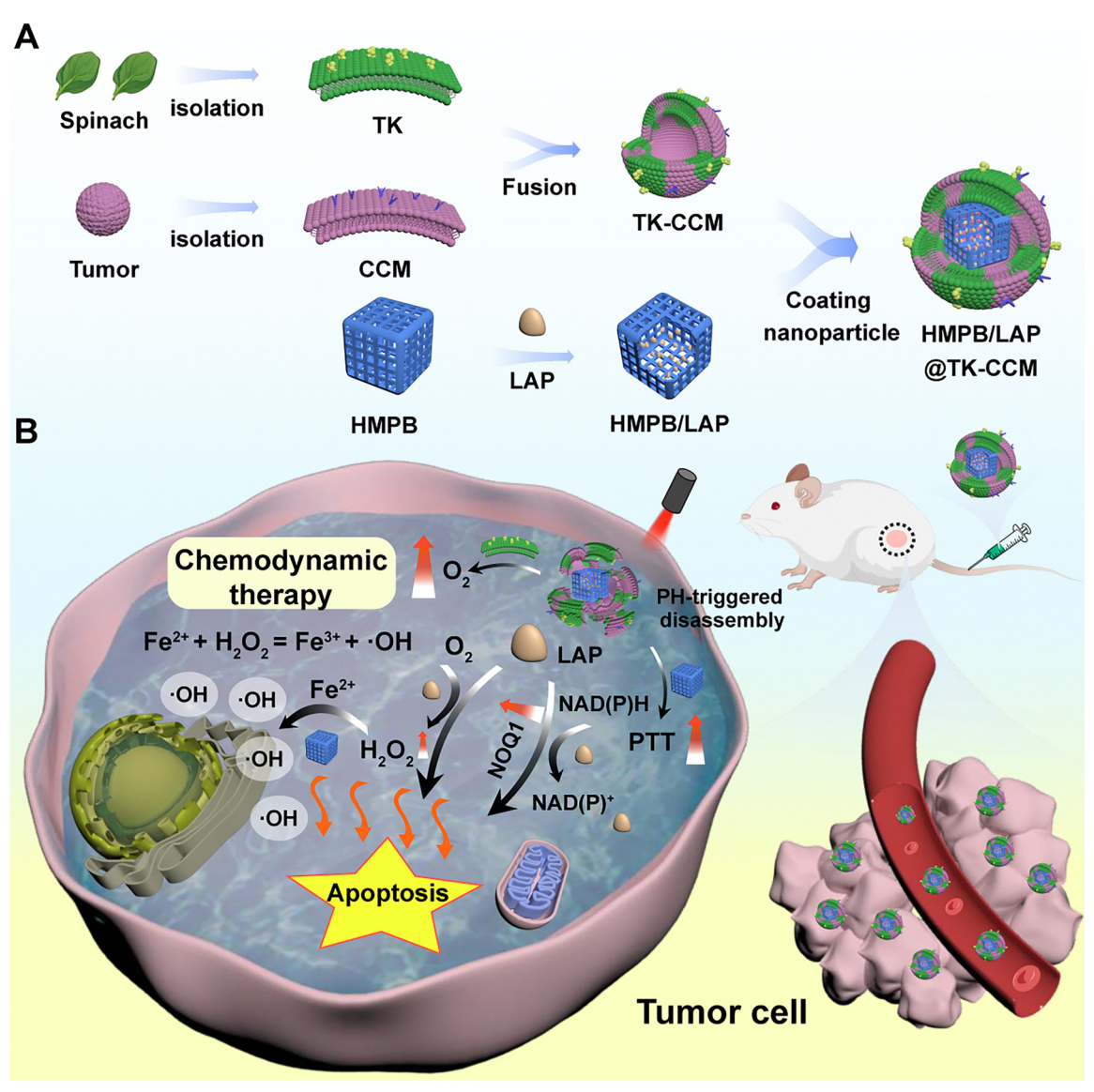
[†] Electronic supplementary information (ESI) available. See DOI: https://doi.org/ 10.1039/d5nh00110b

[‡] C. M. Huo, P. L. Ding, and S. Y. Tong contributed equally to this work.

tumors, positioning LAP as an ideal candidate for enhancing intracellular H₂O₂ levels. 14-17 Prussian blue (PB) is an FDAapproved drug traditionally used for toxin exposure and radioactive contamination. 18-21 It can be synthesized from [Fe(CN)₆]³⁻ and Fe(III) and has the potential to decompose H2O2 into OH through the Fenton reaction. 22-24 Additionally, PB's strong photothermal conversion properties can enhance the Fenton reaction rate by increasing the temperature at tumor sites. 25,26 Combining LAP and PB with nano-catalytic therapy could significantly enhance cancer treatment outcomes by greatly increasing oxidative stress in tumor cells.

Cell membrane camouflage technology has the potential to significantly enhance the targeted delivery efficiency of drugs, thereby improving their overall utilization rate.²⁷⁻³⁰ To facilitate the effective delivery of nanozymes to tumor sites, a hybrid membrane was developed, incorporating both cancer cell membranes and spinach-derived thylakoid (TK) membranes.²⁸ The TK membrane exhibits catalase-like properties that catalytically decompose H₂O₂ into oxygen, alleviating hypoxia in the tumor microenvironment and thereby enhancing the efficacy of PB/ LAP-based nano-catalytic therapy. 31,32 Additionally, the oxygen produced by the TK membrane facilitates the generation of hydrogen peroxide by β-lapachone (LAP), further promoting the Fenton reaction and enhancing the therapeutic synergy of the combined treatment.

In this study, we introduce a hybrid membrane-camouflaged hollow mesoporous Prussian blue (HMPB) nanocatalyst loaded with β-lapachone (HMPB/LAP@TK-CCM), specifically designed for cascade nanocatalysis and amplification of intracellular oxidative stress (Scheme 1). The hybrid membrane provides biomimetic properties, enhancing its tumor-homing ability and immune evasion while mitigating hypoxia in the tumor microenvironment.³³ The hollow mesoporous structure of HMPB allows for a high LAP loading capacity of 120.83%, enabling targeted and sustained drug release. Under acidic and nearinfrared conditions, LAP is rapidly released, continuously



Scheme 1 Schematic diagram of the synthesis and anti-tumor mechanism of HMPB/LAP@TK-CCM.

Nanoscale Horizons Communication

producing H₂O₂ to supply substrates for the Fenton-like reaction of HMPB and promote the generation of radical *OH. This work demonstrates an improved tumor-selective nano-catalytic therapy targeting NQO1-overexpressing tumors, effectively inducing intratumoral oxidative stress while minimizing side effects.³⁴ This nanozyme-based therapeutic system presents a promising and novel approach for clinical applications in breast cancer treatment.

Results and discussion

Preparation and characterization of HMPB/LAP@TK-CCM

In this study, hollow mesoporous Prussian blue nanoparticles (HMPB NPs) were prepared by acid etching PB NPs. The morphology of PB NPs and HMPB NPs was characterized using TEM, revealing that both were cubic in shape, with HMPB NPs displaying a hollow mesoporous structure (Fig. 1(A) and (B)). After etching with hydrochloric acid, the hydrated particle size of NPs remained almost unchanged (Fig. 1(C)). The successful loading of LAP into HMPB was confirmed by measuring the UV absorption peaks at \sim 450 nm (Fig. 1(D)). The hollow mesoporous structure of HMPB NPs provided room for LAP loading. The drug loading content and encapsulation efficiency were calculated based on the standard curve of LAP (Fig. S1, ESI†). As shown in Fig. S2 (ESI†), the nitrogen adsorption-desorption isotherm of HMPB displayed a type IV isotherm with a hysteresis loop (relative pressure 0.4-1.0), confirming its mesoporous structure. BET analysis showed that the specific surface area increased from

58.2 m² g⁻¹ (PB) to 119.7 m² g⁻¹ after etching, indicating successful mesopore formation. The average pore diameter was 16.4 nm, favorable for drug loading. After LAP loading, the pore size decreased to 8.0 nm, verifying effective drug encapsulation in mesopores. The drug loading capacity reached \sim 120.83% and the encapsulation capacity was 60.47% when the LAP concentration was 48 µg mL⁻¹ (Fig. 1(E) and (F)). In addition, to minimize drug leakage, HMPB/LAP was coated with a hybrid membrane (TK-CCM) to obtain HMPB/LAP@TK-CCM. HMPB NPs were covered with TK-CCM to enhance their tumor-targeting capability and physiological stability. Membrane structure and successful membrane decoration were clearly observed via TEM (Fig. 1(G)). According to the sodium dodecyl sulfate-polyacrylamide gel electrophoresis (SDS-PAGE) results, the representative proteins in the two kinds of membranes were both observed in the HMPB/ LAP@TK-CCM group (Fig. 1(H)). Upon membrane coating, the hydrated particle size of HMPB/LAP@TK-CCM increased from 209.6 nm (HMPB/LAP NPs) to 265.3 nm, and the zeta potential changed from -16.4 to -13 mV, which was close to the hybrid membrane alone (-12.6 mV), indicating the successful preparation of HMPB/LAP@TK-CCM NPs (Fig. S3, ESI†). We assessed the colloidal stability of HMPB/LAP@TK-CCM in biological media via time-dependent dynamic light scattering (DLS) measurements. As shown in Fig. S4 (ESI†), the hydrodynamic diameter remained stable in PBS, FBS, and DMEM over 24 hours, confirming excellent dispersion and stability across physiological environments. These results validate the nanoplatform's suitability for biological applications.

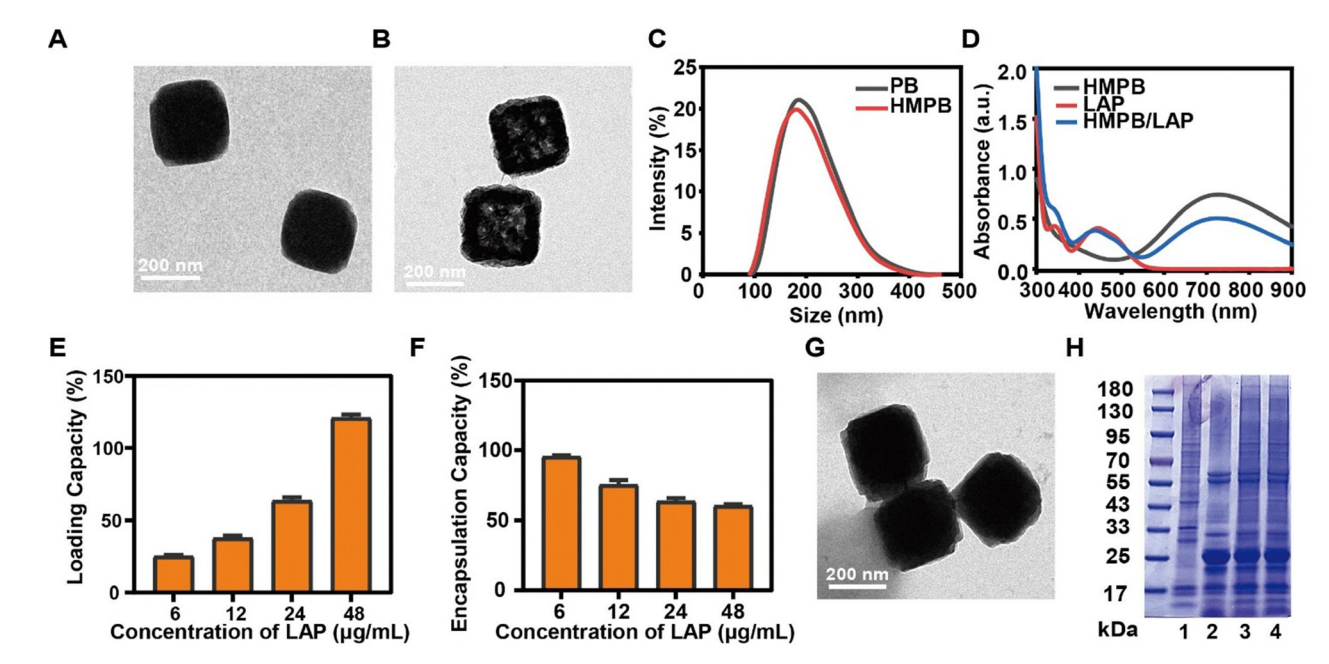


Fig. 1 TEM images of (A) PB and (B) HMPB NPs (scale bar: 200 nm). (C) Size distributions of PB and HMPB NPs. (D) The UV-vis absorption spectra of HMPB NPs, LAP, and HMPB/LAP NPs. (E) LAP loading capacity of HMPB NPs when the LAP concentration was 6, 12, 24, and 48 μg mL⁻¹, respectively. (F) LAP encapsulation capacity when the LAP concentration was 6, 12, 24, and 48 μg mL $^{-1}$, respectively. (G) TEM image of HMPB/LAP@TK-CCM. Scale bar: 200 nm. (H) SDS-PAGE protein analysis in different formulations (1: CCM, 2: TK, 3: TK-CCM, 4: HMPB/LAP@TK-CCM).

Communication

In vitro photothermal performance

808 nm is one of the most frequently used wavelengths for the NIR laser in photothermal tumor ablation. Thus, to study the in vitro photothermal performance, HMPB@TK-CCM NP solution was irradiated with an 808 nm near-infrared laser at a power density of 1.0 W cm⁻², with water and HMPB NP solution used as controls. After 5 min of irradiation, the temperature of the water only increased by 3.4 $^{\circ}$ C, while HMPB@TK-CCM NPs exhibited a significant temperature rise (23.4 °C to 62.9 °C) under NIR irradiation (Fig. 2(A) and (B)). Furthermore, the photothermal conversion efficiency of HMPB@TK-CCM NPs was nearly identical to that of HMPB NPs, indicating that the encapsulation of the hybrid membrane had little impact on the photothermal effect of HMPB NPs. In addition, Fig. 2(C) indicates the stable temperature change of HMPB@TK-CCM NP solution after 5 on-off cycles, which is the key property to confirm the photothermal efficacy. There was an insignificant decrease in the maximal temperature after five cycles of irradiation (10 min for each cycle), indicating the excellent photothermal stability of HMPB@TK-CCM NPs. Notably, although morphological disruption was observed after laser irradiation (Fig. S5, ESI†), the photothermal cycling experiments still exhibited consistent temperature elevation, indicating that the intrinsic photothermal activity of the HMPB core was largely preserved despite partial structural degradation. Additionally, the photothermal conversion efficiency (n) of HMPB@TK-CCM NPs was calculated to be 27.2% based on the heating-cooling curve (Fig. S6, ESI†). These findings collectively affirmed the excellent photothermal performance of HMPB@TK-CCM NPs, which makes them suitable as an efficient photothermal agent in the near-infrared I window.

In vitro Fenton performance

To study the in vitro Fenton performance of HMPB NPs, the peroxidase (POD) activity of the HMPB NPs at acidic pH was examined using 3,3',5,5'-tetramethylbenzidine (TMB) as a

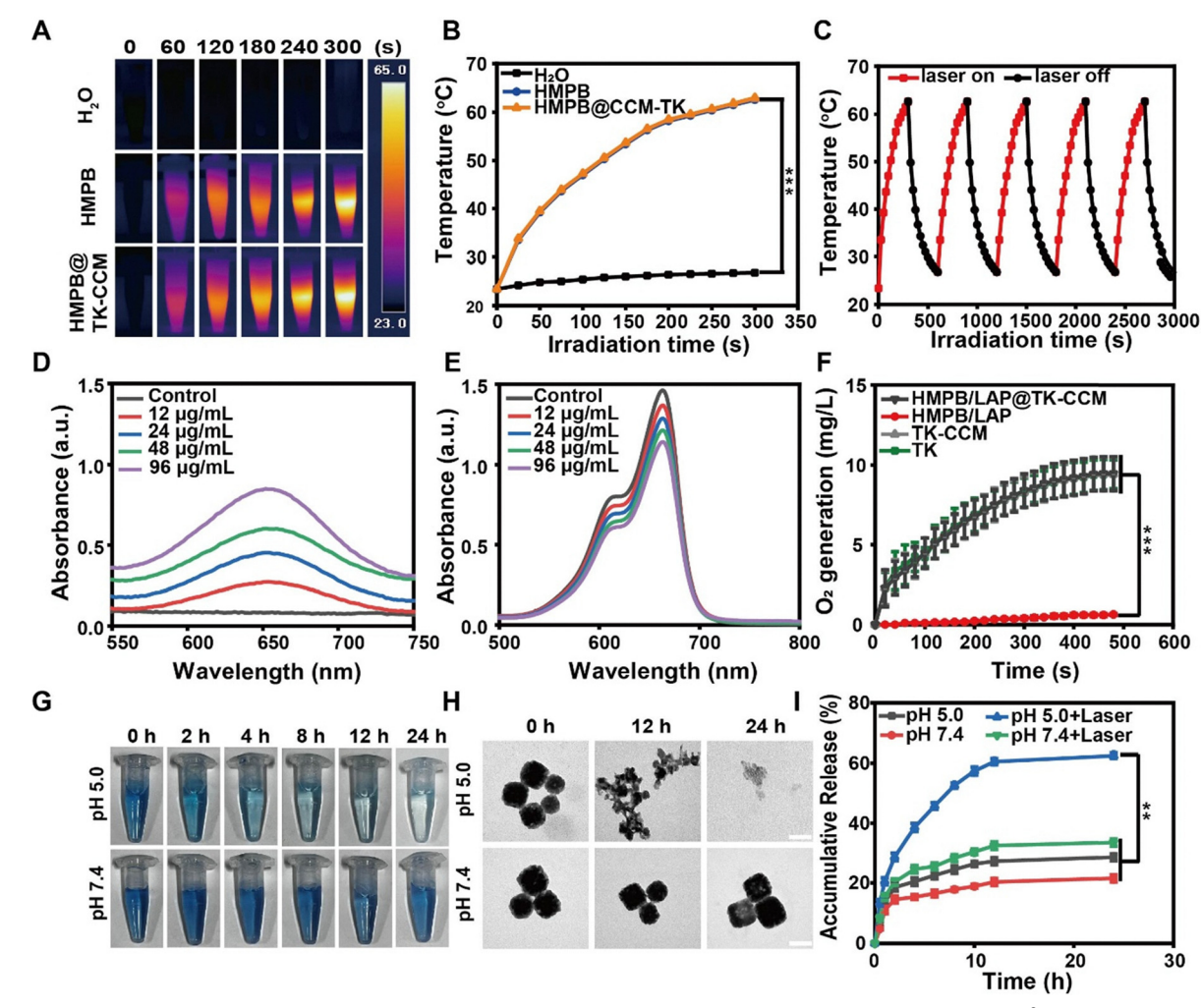


Fig. 2 (A) Infrared thermal images and (B) temperature curves of different samples with 808 nm laser irradiation (1.0 W cm⁻²) for 5 min. (C) Photostability of HMPB@TK-CCM under 808 nm laser irradiation for 5 times. (D) UV-vis absorption of the chromogenic reaction of TMB at different HMPB NP concentrations. (E) UV-vis absorption of degraded MB at different HMPB NP concentrations. (F) O2 generation of TK, TK-CCM, HMPB/LAP, HMPB/ LAP@TK-CCM in the presence of H_2O_2 (n = 3). (G) Changes in HMPB solutions with varying pH values over time. (H) TEM images of HMPB in PBS at pH 5.0 and 7.4 for 0, 12, and 24 h. (I) LAP release from HMPB/LAP@TK-CCM NPs at pH 5.0 and 7.4 with or without 808 nm laser irradiation (1.0 W cm⁻²).

chromogenic reagent. TMB can be oxidized by hydroxyl radicals (*OH), generating a blue product (TMB-ox) with maximal absorbance at 653 nm (Fig. S7, ESI†). The results showed that the OD values of the solution at 653 nm increased with the concentration of HMPB NP solution (Fig. 2(D)), indicating a positive correlation between the production of TMB-ox and concentration of HMPB NPs.

Nanoscale Horizons

Furthermore, the ability of HMPB NPs to generate OH was further assessed using methylene blue (MB) as an indicator. MB can be oxidized by OH, leading to a decrease in its OD value at 663 nm. As shown in Fig. 2(E), the OD values of the HMPB solution at 663 nm decreased with an increased concentration of HMPB NPs. Collectively, the above results indicated that HMPB NPs could efficiently convert H₂O₂ into OH.

To elucidate the role of each component in this catalytic process, control experiments were performed to compare the Fenton-like activity of HMPB/LAP@TK-CCM, HMPB NPs, and TK membranes (TK-M) using TMB as an indicator (Fig. S8, ESI†). The data showed that HMPB/LAP@TK-CCM and HMPB NPs displayed comparable catalytic performance, whereas TK-M exhibited negligible activity. These data suggest that the Fenton-like catalytic performance mainly originates from the HMPB core, and the presence of the TK membrane does not significantly impair this activity.

Given the potential of tumor-localized hyperthermia induced by NIR irradiation, we further assessed the OH generation of the nanoplatform under mild heating conditions (45 °C) to simulate this photothermal effect. As illustrated in Fig. S9 (ESI†), a slight increase in TMB-ox absorbance was observed at elevated temperature, suggesting that hyperthermia can further enhance Fenton-like activity, likely by accelerating H₂O₂ decomposition and promoting reactive species formation.

Moreover, considering that the TK possesses inherent catalase-like properties that may impact the availability of H₂O₂, we conducted a comparative analysis of *OH generation in the presence and absence of TK membranes. As shown in Fig. S10 (ESI†), both HMPB/LAP@TK-CCM and HMPB/LAP@CCM showed comparable TMB oxidation efficiencies, with only a slight reduction in the TK-coated group. These results indicate that the catalytic activity of the system is largely preserved despite the TK-mediated H2O2 decomposition under experimental conditions.

Notably, the inclusion of TK not only preserves Fenton efficiency but also contributes beneficially by generating oxygen, which may help alleviate tumor hypoxia and support β-lapachone-induced ROS amplification through redox cycling. Collectively, these findings demonstrate that HMPB/LAP@ TK-CCM retains strong OH generation capability under acidic, oxidative, and thermally elevated tumor-mimicking conditions, indicating its potential as a robust chemodynamic therapeutic platform.

In vitro oxygen production performance

Thanks to the catalase-like activity of TK and the elevated H₂O₂ levels in the tumor microenvironment, HMPB/LAP@TK-CCM can catalyze the production of O2 from H2O2, resulting in membrane rupture and alleviating tumor hypoxia. As shown in Fig. 2(F) and Fig. S11 (ESI†), under simulated TME conditions, the hybrid membrane-modified NPs could rapidly generate O2. Importantly, HMPB/LAP@TK-CCM exhibits a similar oxygen production rate to TK and TK-CCM, while HMPB/LAP hardly produces O2, further confirming that HMPB/LAP@TK-CCM retains the inherited catalase from TK.

In vitro acid-triggered degradation performance

Under pH 5.0 conditions (simulating an acidic endosome), the biodegradation of HMPB NPs was studied by monitoring changes in solution color and NP morphology, with pH 7.4 serving as a control. As presented in Fig. 2(G), under pH 5.0 conditions, HMPB NPs changed from deep blue (0 h) to nearly colorless (24 h). TEM images revealed the presence of very small fragments (Fig. 2(H)), suggesting the biodegradation of HMPB NPs during the endocytosis process. However, insignificant color and morphology changes were observed at pH 7.4. Subsequently, the leaching kinetics of iron ions were investigated. The results indicated that HMPB NPs released more iron ions under low pH conditions (pH 5.0) compared to neutral pH conditions (pH 7.4), highlighting the pH dependency of HMPB NPs (Fig. S12, ESI†).

In vitro drug release

The drug release profile of HMPB/LAP@TK-CCM was systematically evaluated under a series of tumor-relevant stimuli, including acidic pH, oxidative stress, high intracellular glutathione (GSH) levels, and near-infrared (NIR) irradiation. As shown in Fig. 2(I), the release rate of LAP was significantly accelerated under acidic conditions (pH 5.0) compared to physiological pH (pH 7.4) and was further enhanced upon NIR laser exposure. These results suggest that the LAP release is jointly triggered by the mildly acidic environment and externally applied photothermal stimulation, the former being a hallmark of the tumor microenvironment and the latter representing a controllable therapeutic cue.

To further explore the redox-responsive behavior of the nanoplatform, in vitro release experiments were conducted in the presence of 10 mM glutathione (GSH), mimicking the elevated intracellular GSH concentrations typically found in tumor cells. As illustrated in Fig. S13 (ESI†), the presence of GSH markedly accelerated LAP release, which can be attributed to its ability to reduce Fe³⁺ in the HMPB framework to Fe²⁺, leading to structural destabilization and enhanced drug diffusion.

Moreover, the influence of oxidative stimuli was investigated by introducing hydrogen peroxide (H2O2, 100 µM), which is commonly upregulated in tumor tissues. As shown in Fig. S14 (ESI†), H₂O₂ exposure under acidic conditions further accelerated LAP release, suggesting that the oxidative environment facilitates the degradation of the HMPB framework. This is consistent with the Fenton-like activity of HMPB, which catalyzes the generation of hydroxyl radicals and promotes nanostructure decomposition.

Taken together, these results confirm that HMPB/LAP@TK-CCM exhibits a multi-stimuli-responsive drug release profile, sensitively regulated by pH, redox conditions (GSH and H₂O₂), and NIR irradiation. The integration of these tumor-specific triggers enables precise control over drug release kinetics, thereby improving the therapeutic selectivity and minimizing off-target effects.

In vitro targeting study

To investigate the internalization of NPs by different cells, Cy5labeled HMPB@TK, HMPB@CCM, and HMPB@TK-CCM NPs were co-incubated with 4T1 or 3T3 cells for 4 h, respectively. Qualitative and quantitative studies of homologous targeting of HMPB/LAP@TK-CCM were performed using confocal laser scanning microscopy (CLSM) and flow cytometry. Compared with the HMPB@TK-Cy5 treated group, 4T1 cells treated with HMPB@CCM-Cy5 and HMPB@TK-CCM-Cy5 had obvious and similar red fluorescence (Fig. 3(A)). Moreover, compared to the HMPB@TK-Cy5 treated groups, there were notable differences in the uptake of HMPB@TK-CCM-Cy5 among the various cell

lines (Fig. 3(A) and (B)). The corresponding quantitative results showed that the average fluorescence intensity in homologous 4T1 cells indicated a significantly enhanced cellular uptake efficiency of HMPB@TK-CCM-Cy5, with approximately a 3.6fold increase compared to 3T3 cells (Fig. 3(C) and (D)). These results demonstrated that HMPB@TK-CCM NPs have excellent targeting capabilities toward homotypic cancer cells.

In vitro antitumor activity

The generation of ROS is a crucial aspect of CDT. To examine whether HMPB/LAP@TK-CCM NPs could induce ROS production, we used DCFH-DA to detect the ROS levels in 4T1 cells. DCFH-DA converts to 2',7'-dichlorofluorescein (DCF) in response to stimulation by intracellular ROS. As shown in Fig. 4(A), the green fluorescence in the HMPB/LAP@TK-CCM + H₂O₂ group was significantly higher than that in both the control and H2O2 groups, indicating that HMPB/LAP@TK-CCM NPs exhibited strong peroxidase (POD) activity and effectively produced a substantial amount of ROS. Furthermore, the green fluorescence in the HMPB/LAP@TK-CCM + H2O2 + NIR

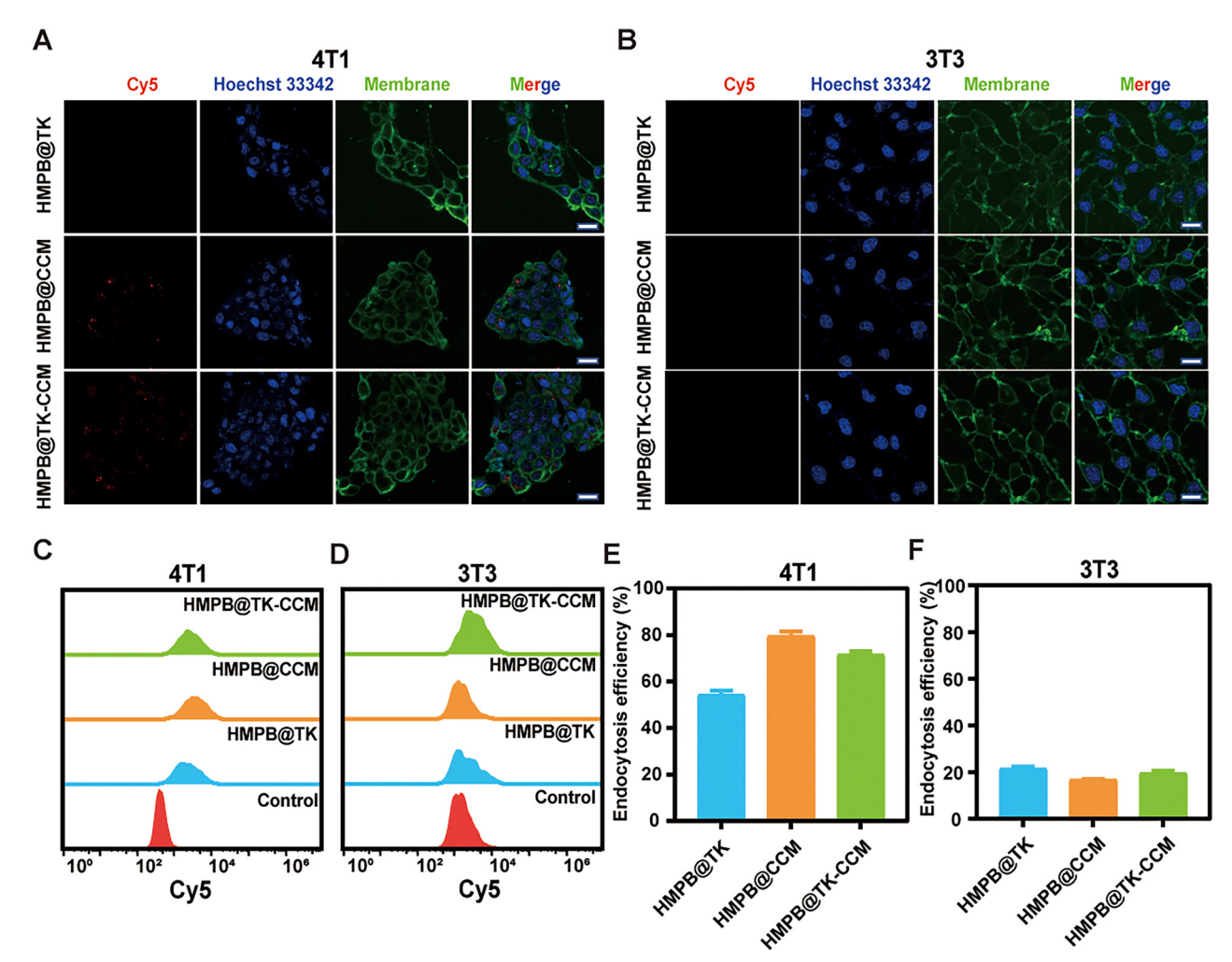


Fig. 3 CLSM images of (A) 4T1 cells and (B) 3T3 cells co-incubated with Cy5-labeled HMPB@TK, HMPB@CCM, and HMPB@TK-CCM NPs for 4 h. Scale bar: 10 µm. (C, D) Flow cytometry analysis and (E, F) endocytosis efficiency of 4T1 and 3T3 cells co-incubated with Cy5-labeled HMPB@TK, HMPB@CCM, and HMPB@TK-CCM NPs for 4 h (n = 3).

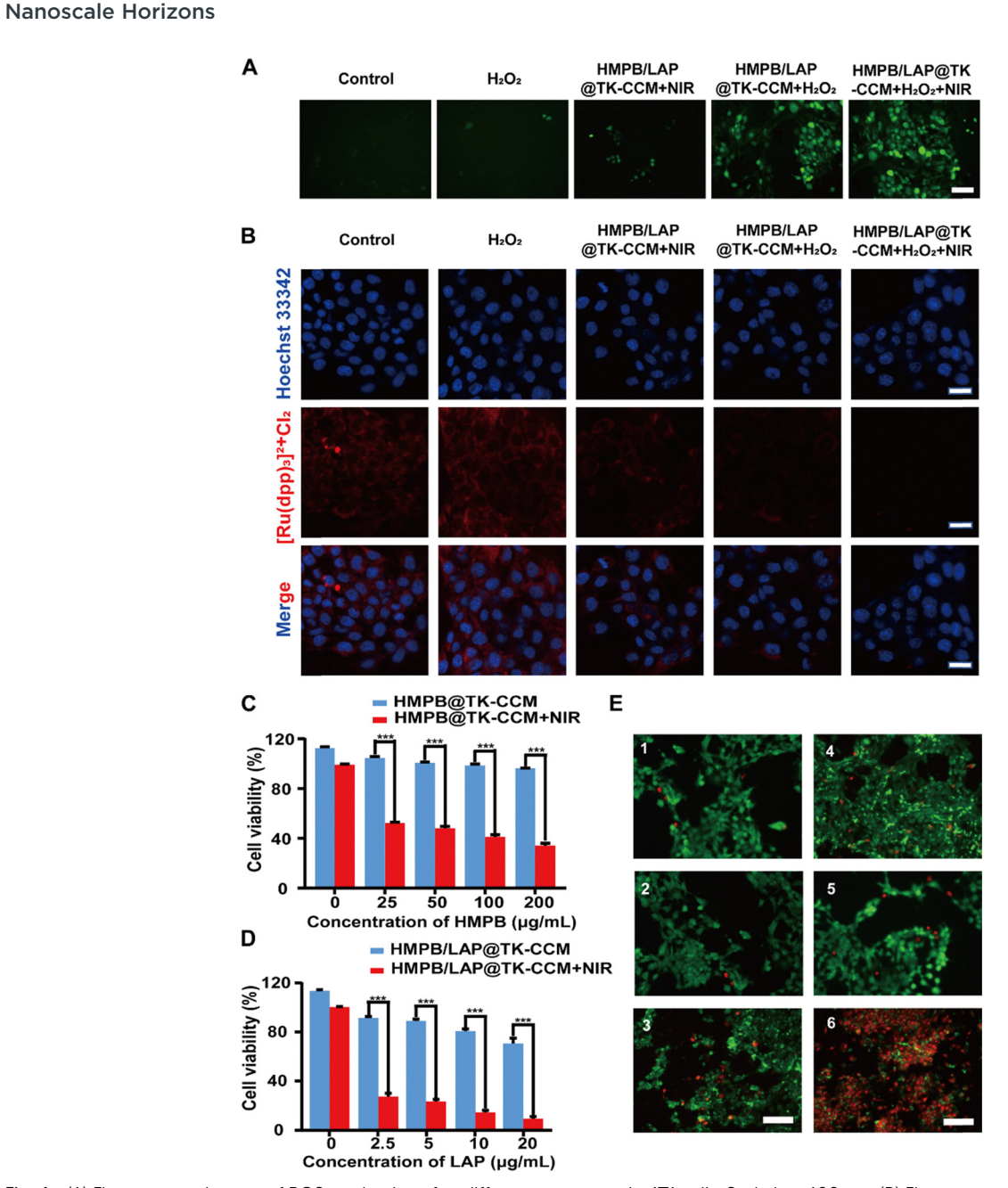


Fig. 4 (A) Fluorescence images of ROS production after different treatments in 4T1 cells. Scale bar: 100 μm. (B) Fluorescence images of 4T1 cells using [Ru(dpp)₃]²⁺Cl₂ as an intracellular hypoxia probe. Scale bar: 10 μm. (C) The quantitative assay of cell viability after different treatments: HMPB@TK-CCM; HMPB@TK-CCM + NIR (1.0 W cm $^{-2}$, 5 min) (n = 3). (D) The quantitative assay of cell viability after different treatments: HMPB/LAP@TK-CCM; HMPB/ LAP@TK-CCM + NIR (1.0 W cm $^{-2}$, 5 min) (n = 3). (E) Live/dead staining of 4T1 cells after different treatments: (1) NIR Laser, (2) HMPB@TK-CCM NPs, (3) HMPB@TK-CCM NPs + Laser (1.0 W cm⁻², 5 min), (4) LAP, (5) HMPB/LAP@TK-CCM NPs, (6) HMPB/LAP@TK-CCM NPs + Laser (1.0 W cm⁻², 5 min), Scale bar: 100 µm.

group was further enhanced, possibly due to the increased ROS generation by HMPB/LAP@TK-CCM NPs under NIR irradiation. This observation aligns with earlier findings in our study showing that mild hyperthermia (45 °C) promotes OH generation (Fig. S9, ESI†), further supporting the thermally enhanced catalytic behavior of the system.

In parallel, intracellular H₂O₂ levels were quantified using a hydrogen peroxide assay kit to clarify whether the ROS increase resulted from enhanced H₂O₂ production or its efficient

consumption (Fig. S15, ESI†). Interestingly, H₂O₂ levels in HMPB/LAP@TK-CCM-treated cells were significantly reduced, suggesting rapid consumption of H₂O₂ through the Fenton-like reaction catalyzed by the HMPB core. These results indicate that H₂O₂ generated via NQO1-mediated β-lapachone activation is effectively utilized in situ, contributing to ROS amplification while avoiding excess accumulation.

We next studied the hypoxia modulation by HMPB/LAP@ TK-CCM NPs in 4T1 cells. Intracellular hypoxia was assessed

using [Ru(dpp)₃]²⁺Cl₂ as a probe, whose fluorescence is significantly quenched by O₂. As shown in Fig. 4(B), the red fluorescence in the HMPB/LAP@TK-CCM + NIR group was weaker than that in both the control and H₂O₂ groups, indicating the POD activity of HMPB/LAP@TK-CCM NPs. To better simulate the tumor microenvironment, the POD activity of HMPB/LAP@TK-CCM was further enhanced with the addition of 100 μM H₂O₂. Notably, under the combined effects of NIR and H2O2, HMPB/LAP@TK-CCM exhibited negligible red fluorescence. This may be attributed to the natural catalase present in TK, which catalyzes the decomposition of H₂O₂ to produce oxygen, thus alleviating hypoxia.

Cell toxicity was assessed using the CCK-8 method to evaluate the impact of NPs on different cells. As shown in Fig. S16 (ESI†), the survival rate of 3T3 cells treated with HMPB@ TK-CCM NPs was above 95%, which indicated that the HMPB@ TK-CCM NPs have good biocompatibility with normal cells. Furthermore, to assess photothermal safety, the phototoxicity of HMPB/LAP@TK-CCM was examined in 3T3 cells under laser irradiation (808 nm, 1.0 W cm⁻², 5 min). As shown in Fig. S17 (ESI†), the viability of 3T3 cells remained above 80% across all tested concentrations, suggesting minimal photothermal cytotoxicity. This favorable outcome is likely attributed to the homologous targeting capability conferred by the 4T1-derived membrane, which enhances selective accumulation in tumor cells while sparing normal cells, thereby improving the tumor

specificity and biosafety of the nanoplatform. Fig. 4(C) and (D) indicates that both HMPB@TK-CCM and HMPB/LAP@TK-CCM exhibited some cytotoxicity towards the 4T1 cells. This may be due to the homologous cell targeting, which enhanced the cellular internalization of NPs and facilitated the generation of OH through the Fenton reaction while LAP release further augmented this process. Upon NIR irradiation, cell viability declined sharply in both the HMPB@TK-CCM and HMPB/ LAP@TK-CCM groups, principally due to the following two reasons: (1) photothermal ablation cells induced by photothermal conversion performance of PB and (2) photothermal conversion enhanced the Fenton reaction rate by increasing the temperature.

The live/dead staining images further confirmed the above CCK-8 outcomes. As illustrated in Fig. 4(E), nearly all the cells treated with HMPB/LAP@TK-CCM NPs under 808 nm laser irradiation were apoptotic or dead, as indicated by the red fluorescence of propidium iodide (PI). In contrast, many living cells with green fluorescence were still visible in the control groups. Thus, HMPB/LAP@TK-CCM NPs, combined with PTT and CDT, demonstrate superior in vitro antitumor efficacy.

In vivo imaging

Tumor targeting is essential for the desirable antitumor effect, and the in vivo distribution of NPs was evaluated via

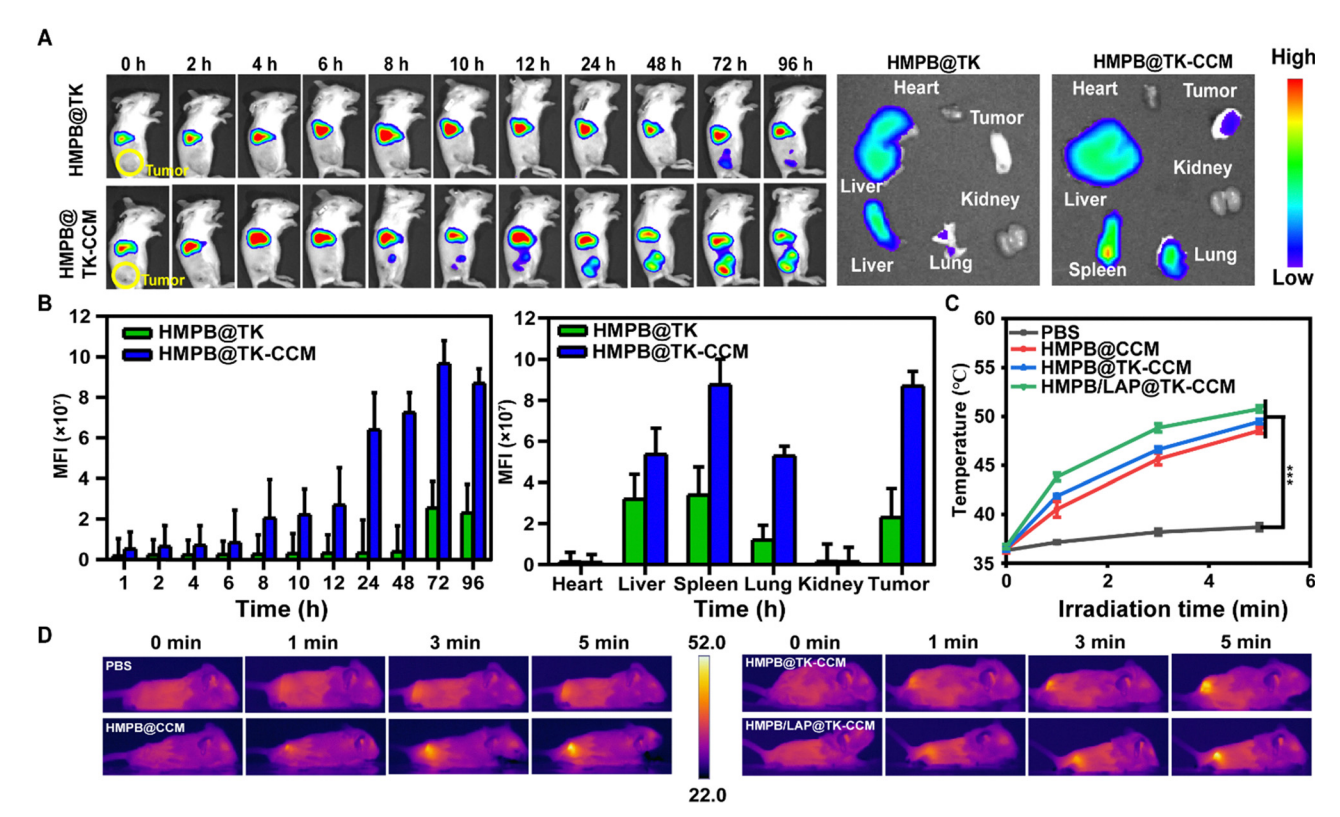


Fig. 5 (A) In vivo fluorescence images of 4T1 tumor-bearing BALB/c mice at different time points after intravenous injection of NPs and the corresponding fluorescence images of major organs and tumors harvested at 96 h post-administration. (B) Quantitative analysis of fluorescence intensity of tumors at certain time points, and the mean fluorescence intensity of ex vivo tumors and organs at 96 h post-injection. (C) Temperature increase profiles for laser-illuminated tumor tissues as a function of irradiation time. ***p < 0.001. (D) In vivo photothermal images of 4T1 tumor-bearing mice after intravenous injection with PBS, HMPB@CCM, HMPB@TK-CCM and HMPB/LAP@TK-CCM with 808 nm laser irradiation.

Nanoscale Horizons Communication

fluorescence imaging in 4T1-tumor-bearing mice. As demonstrated in Fig. 5(A) and (B), the DiR-labeled HMPB@TK-CCM NP group exhibited a noticeable fluorescence signal at the 4T1 tumor site 10 h after intravenous injection. Over time, the accumulation at tumor sites became more pronounced, with the strongest signal observed 72 hours post-administration. In contrast, the fluorescence signal at the tumor site in the DiRlabeled HMPB@TK NP group remained weak, with no sustained accumulation. These results demonstrate the specific tumor-targeting ability of HMPB@TK-CCM for homologous

tumors. The mice were sacrificed 96 h post-administration, and tumors and major organs were harvested for fluorescence quantification. Ex vivo fluorescence analysis showed that the tumor-targeting efficacy of HMPB@TK-CCM NPs was significantly greater than that of HMPB@TK NPs. Furthermore, infrared thermal imaging revealed that the temperature at the tumor site in the HMPB/LAP@TK-CCM group increased from 37 °C to nearly 50 °C within 5 min of 808 nm laser irradiation (Fig. 5(C) and (D)), while the PBS treatment group maintained a temperature of 37 °C. Taken together, these results confirm

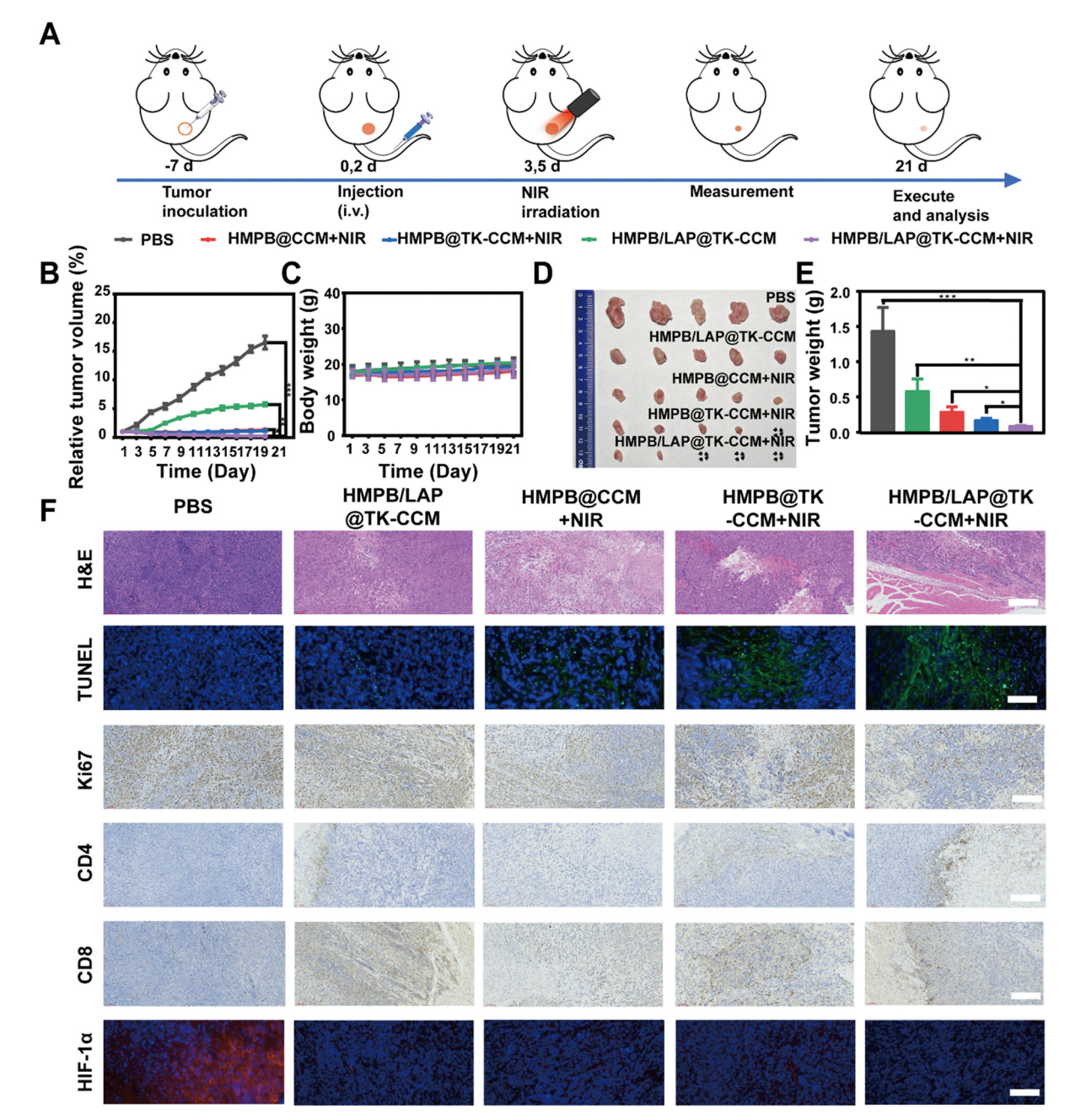


Fig. 6 (A) Treatment schedule of collaborative tumor treatment. (B) Relative tumor volume curves and (C) body weight of mice in different treatment groups during the 21-day treatment period (n = 5). (D) Pictures of the excised tumors at the therapeutic endpoint. (E) Mean tumor weights of 4T1 tumors removed from the mice in different groups (n = 5). (F) H&E, Ki67, CD4, CD8 immunohistochemical, TUNEL, and HIF- 1α immunofluorescence staining images of tumor issues in different treatment groups after treatment completion. Scale bar: 100 µm.

that HMPB/LAP@TK-CCM NPs can effectively accumulate at the tumor site and induce irreversible thermal ablation under laser irradiation.

In vivo anti-tumor therapy

Encouraged by the excellent in vitro anti-tumor effects of HMPB/LAP@TK-CCM NPs, a 4T1 tumor-bearing mouse model was established to further assess their in vivo therapeutic efficacy. The tumor-bearing mice were randomly divided into 5 groups (5 mice per group): (1) PBS; (2) HMPB/LAP@TK-CCM; (3) HMPB@CCM + NIR; (4) HMPB@TK-CCM + NIR; and (5) HMPB/LAP@TK-CCM + NIR. 808 nm laser irradiation (1.0 W cm⁻², 5 min) was performed 72 hours after intravenous injection. The tumor size and body weight were measured every other day, and the treatment regimens are shown in Fig. 6(A). After different treatments, all groups exhibited some level of tumor therapeutic effects. Tumor growth was inhibited to

varying degrees in the HMPB/LAP@TK-CCM, HMPB@CCM + NIR, and HMPB@TK-CCM + NIR groups. Notably, the HMPB/ LAP@TK-CCM + NIR group showed the most pronounced tumor suppression, with the relative tumor volume reduced to 0.25 mm³ after 21 days of treatment, likely due to the synergistic effects of CDT and PTT (Fig. 6(B) and Fig. S18, ESI†). Additionally, there were no significant fluctuations in the body weight of mice in any group throughout the treatment period (Fig. 6(C)), indicating the good biocompatibility of our nanozymes.

At the end of the treatment, the mice were dissected, and their tumor tissues were collected, photographed, and weighed. The results further demonstrated the superior therapeutic effect of the HMPB/LAP@TK-CCM + NIR group (Fig. 6(D) and (E)), underscoring the specific targeting capability of HMPB/ LAP@TK-CCM and its substantial tumor growth inhibitory effects under NIR irradiation. Further evaluation of the effects of different treatments was conducted through H&E staining,

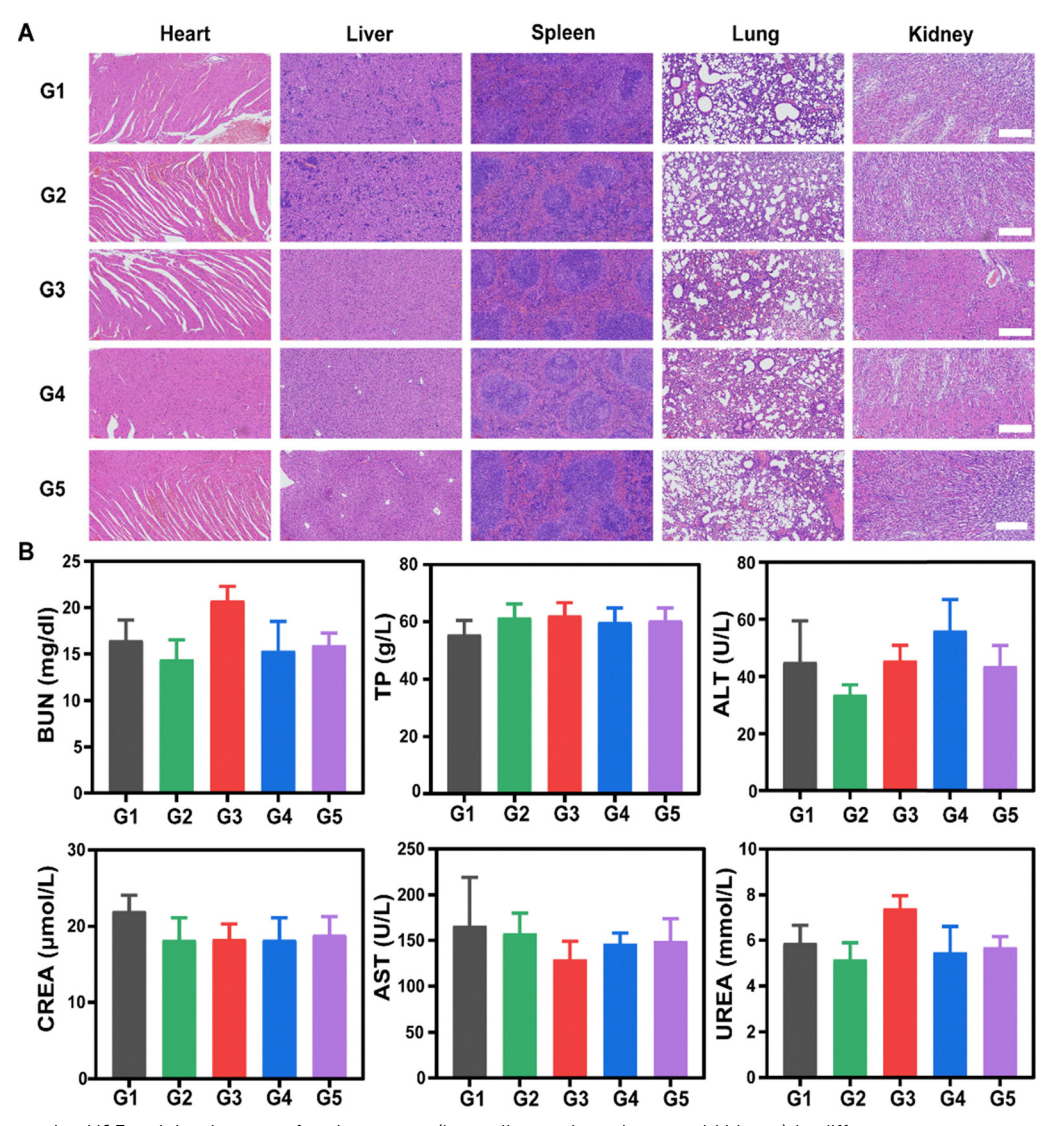


Fig. 7 (A) Representative H&E staining images of major organs (heart, liver, spleen, lung, and kidneys) in different treatment groups after treatment completion. Scale bar: 100 µm. (B) Blood biochemical analysis in different treatment groups after treatment completion. (G1) PBS; (G2) HMPB/LAP@TK-CCM; (G3) HMPB@CCM + NIR; (G4) HMPB@TK-CCM + NIR; (G5) HMPB/LAP@TK-CCM + NIR (n = 3).

Ki67 immunohistochemistry, and terminal deoxynucleotidyl transferase-mediated dUTP nick-end labeling (TUNEL) immunofluorescence staining (Fig. 6(F)). H&E staining of tumor sections showed nuclear condensation and cell death in all treatment groups compared to the PBS group, with the most pronounced effect observed in the HMPB/LAP@TK-CCM + NIR group. Additionally, apoptosis in tumor tissue from the HMPB/LAP@TK-CCM + NIR group was further assessed using the TUNEL assay, revealing significantly higher levels of apoptosis (green fluorescence) compared to mice treated with PBS or HMPB/LAP@TK-CCM NPs. The Ki67 assay further confirmed that this group had the

We further investigated whether PTT combined with CDT could trigger an antitumor immune response. Immunohistochemistry results of CD4 and CD8 staining in tumor sections showed that all treatment groups had increased induction of CD4⁺ and CD8⁺ T cells compared to the control group, with enhanced infiltration rates in tumor tissue. The HMPB/LAP@ TK-CCM + NIR group exhibited the highest infiltration rate. Overall, tumor cells treated with CDT combined with PTT improve the proliferation and activation of T cells effective for tumor therapy. Hypoxia inducible factor- 1α (HIF- 1α), as an endogenous indicator, can also reflect the intratumoral hypoxia level. The red fluorescence signals of HIF-1α in the PBS group showed strong intensity, suggesting significant hypoxia in the 4T1 tumor model. In contrast, the HMPB/LAP@TK-CCM + NIR group displayed the strongest ability to down-regulate HIF- 1α expression. This effect is likely due to HMPB/LAP@TK-CCM NPs increasing the temperature in the tumor region under NIR irradiation, which enhances blood flow and alleviates tumor hypoxia. Additionally, TK contains natural catalase, which catalytically decomposes the hydrogen peroxide (H₂O₂) in the tumor microenvironment to produce oxygen, further improving the hypoxic environment. Overall, these results collectively demonstrate the high efficacy of combined CDT/PTT therapy by our designed nanozymes.

Biosafety assessment

Nanoscale Horizons

lowest cell proliferation.

Finally, the in vivo toxicity of NPs was evaluated using H&E staining and blood biochemistry tests. As illustrated in Fig. 7(A), H&E staining of major organs (heart, liver, spleen, lung, and kidney) revealed no noticeable abnormalities, indicating that the mice remained healthy after treatment. These results suggest that the toxicity resulting from NP injection is negligible. Moreover, blood biochemical analysis demonstrated that liver function (AST, ALT, TP) and kidney function (CREA, BUN, UREA) in treated mice were within the normal range and not significantly different from the control group, indicating minimal systemic toxicity (Fig. 7(B)). Overall, mice administrated with HMPB/LAP@TK-CCM NPs showed no toxic side effects, highlighting their good biocompatibility and biosafety for potential biomedical applications.

Conclusions

In summary, we successfully developed a biomimetic nanozyme, a hybrid membrane camouflaged hollow mesoporous Prussian blue (HMPB) nanocatalyst loaded with β-lapachone (HMPB/ LAP@TK-CCM) for enhanced nano-catalytic therapy, supported by photothermal therapy (PTT). The nanozyme is infused with the anticancer drug β-lapachone (LAP), which elevates H₂O₂ levels within tumor cells, thereby amplifying the Fenton reaction facilitated by HMPB. The hybrid membrane not only facilitates tumor homing of the NPs but also alleviates hypoxic conditions within the TME, optimizing the therapeutic potential of the nanocatalyst. In vitro cell assays and in vivo anti-tumor experiments confirm that the nanozymes exhibit high therapeutic efficacy and low toxicity. Histological analysis, including H&E staining and TUNEL immunostaining, further demonstrates that the nano-catalytic therapy induces significant tumor cell apoptosis and necrosis. In conclusion, the HMPB/LAP@TK-CCM nanozyme developed in this study offers excellent temperature and pH responsiveness, enabling safe and effective multi-modal therapy, focusing on nano-catalytic chemotherapy for enhanced cancer treatment, with substantial clinical potential. Overall, the HMPB/LAP@TK-CCM nanozyme developed in this study improves nano-catalytic therapy, enhanced by photothermal therapy, demonstrating significant clinical potential.

Materials and methods

Materials and reagents

K₃[Fe(CN)₆]·3H₂O was purchased from Aladdin Biochemical Co., Ltd (China). Poly(N-vinylpyrrolidone) (PVP) was obtained from Yuanye Biotechnology Co., Ltd (China). β-Lapachone (LAP) was purchased from TargetMol Chemicals Inc (America). The cell membrane protein and cytoplasmic protein extraction kit, reactive oxygen species assay kit, and SDS-PAGE gel preparation kit were all provided by Beyotime Biotechnology Co., Ltd (China). HEPES was acquired from Acmec Biochemical Co., Ltd (China). H₂O₂, 3,3',5,5'-tetramethylethyl-benzidine (TMB), and methylene blue (MB) were bought from Aladdin Biochemical Co., Ltd (China). The cell viability (live and dead cell staining) detection kit (KGAF001), RPMI-1640, and DMEM medium (Keygen BioTECH) were obtained from KeyGEN Biotechnology Co., Ltd (China). Fetal bovine serum (FBS), pancreatic enzyme, and penicillin-streptomycin solution were obtained from Gibco Biotechnology Inc. (America). Cell counting kit-8 was obtained from Dojindo Laboratories (Japan). Cell mask™ green plasma and Hoechst 33342 were purchased from Thermo Fisher Scientific Inc. (America). BALB/c mice were obtained from Beijing Vital River Laboratory Animal Technology Co., Ltd (China). All other reagents were of analytical purity and used without further purification.

Preparation of HMPB NPs

Hollow mesoporous Prussian blue NPs (HMPB NPs) were prepared using a hydrothermal acid etching method. The specific procedure is as follows: first, 131.7 mg of K₃[Fe(CN)₆]·3H₂O and 3 g of PVP were added to 40 mL of 0.01 M hydrochloric acid, and after stirring with a magnetic stirrer for 30 min, a clear yellow solution was obtained. Subsequently, the solution was heated at 80 $^{\circ}$ C for 20 h. After heating was complete, the product was centrifuged (12000 rpm, 10 min), washed with water, and vacuum-dried to obtain blue powdery Prussian blue NPs. Next, 20 mg of Prussian blue NPs and 100 mg of PVP were added to 20 mL of 1 M hydrochloric acid. After magnetic stirring for 2 h, the solution was transferred to a high-pressure reaction vessel lined with polytetrafluoroethylene and heated at 140 $^{\circ}$ C for 4 h. Then, the product was centrifuged (12000 rpm,

10 min), washed with water, and vacuum-dried to obtain HMPB NPs.

Preparation of β -lapachone-loaded HMPB NPs (HMPB/LAP NPs)

Communication

β-Lapachone (LAP) dissolved in a mixed solvent of DMSO and water (v/v = 9:1) was slowly added into the HMPB solution dissolved in DMSO under stirring at room temperature and reacted for 24 h. After that, the product was centrifuged (12 000 rpm, 10 min), washed with water, and vacuum-dried to obtain HMPB/LAP NPs.

Extraction of 4T1 cancer cell membranes (CCM)

The extraction of 4T1 cell membranes was performed using a previously established method. The specific steps were as follows: first, 4T1 cells were extensively cultured in a 15 cm diameter cell culture dish. When the cells reached around 80% confluence, the cell culture dish was placed on ice, and the 4T1 cells were scraped off and collected. Subsequently, the collected cell suspension was centrifuged (4 °C, 700 g, 10 min), and the cell membrane protein extraction reagent was added to the pellet. The cell suspension was subjected to three cycles of freeze–thaw. After further centrifugation (4 °C, 700 g, 10 min), the supernatant was collected and centrifuged again (4 °C, 13 000g, 40 min) to obtain the membrane pellet, which was stored at -80 °C.

Extraction of thylakoid membranes (TK)

TK was isolated from fresh spinach according to the previously reported method. First, 100 g of fresh spinach leaves were weighed and washed and then stored at 4 °C overnight. Subsequently, they were homogenized in a juicer with pre-chilled 50 mM HEPES buffer (5 mM magnesium chloride, 50 mM sodium chloride, 0.3 M sucrose, pH 7.6, 300 mL). Then, leaf debris was filtered through ten layers of cheesecloth, and the filtrate was collected and centrifuged (8000 rpm, 10 min) to obtain intact chloroplasts. The chloroplasts were suspended in a low-osmolarity buffer, 10 mM HEPES (pH 8.0), for 2 h, and then centrifuged at 12 000 rpm for 30 min to remove the matrix extraction solution from the supernatant. The precipitate was collected, washed twice with 10 mM HEPES buffer, resuspended in water, and then separated for 5 min under ultrasonic treatment at 4 °C. After centrifugation at 16 000 rpm for 15 min, TK membranes were obtained.

Preparation of HMPB/LAP@TK-CCM NPs

The HMPB/LAP@TK-CCM NPs were prepared using a co-extrusion method. Briefly, the HMPB/LAP aqueous solution (100 μg mL⁻¹, 1 mL) was mixed with TK (500 μg mL⁻¹,

100 μ L) and CCM (500 μ g mL⁻¹, 100 μ L). Subsequently, the mixture was passed through polycarbonate porous membranes with pore sizes of 1 μ m, 0.8 μ m, and 0.4 μ m, each for 10 cycles using an Avanti mini extruder. The extruded mixture was collected and then centrifuged (12 000 rpm, 10 min) to obtain HMPB/LAP@TK-CCM NPs.

Characterization of HMPB/LAP@TK-CCM NPs

Transmission electron microscopy (JEM2100F, JEOL) was employed for the morphological characterization of the prepared NPs. The hydrodynamic diameter and zeta potential of the NPs were measured using a nanoparticle laser sizing instrument (Malvern). The drug loading content of the NPs was determined using a UV-visible spectrophotometer (UV-3600 plus, Shimadzu). The dissolved oxygen concentration in the solution was measured using a portable dissolved oxygen meter (JPB-607A, Shanghai Yidian Scientific Instrument Co., Ltd). Sodium dodecyl sulfate–polyacrylamide gel electrophoresis (SDS-PAGE) was utilized to characterize the membrane proteins of prepared NPs.

Peroxidase enzyme activity assessment of HMPB/LAP@TK-CCM NPs

To detect the activity of peroxidase, hydrogen peroxide (1 mM, $200 \,\mu\text{L}$) was co-incubated with thylakoid membranes (0.1 mg mL $^{-1}$, 2 mL) at room temperature for 2 min. The dissolved oxygen content in the solution was monitored using a portable dissolved oxygen meter.

Biodegradability assessment of HMPB NPs

 $400 \mu g$ of HMPB was dissolved in PBS (pH 7.4 or pH 5.0, 10 mM) and then placed in a water bath (37 °C, 200 rpm). TEM was used to observe the morphology of HMPB at different time intervals (0, 12, and 24 h).

Photothermal performance of HMPB@TK-CCM

The HMPB NPs (0.1 mg mL $^{-1}$, 1 mL) or the HMPB@TK-CCM NPs (0.1 mg mL $^{-1}$, 1 mL) were added to a 1.5 mL Eppendorf tube. The NPs were exposed to an 808 nm laser (1.0 W cm $^{-2}$, 5 min), and an infrared thermal imager (Fotric 225) was used to detect the temperature changes of NP solutions. To characterize the thermal stability of HMPB@TK-CCM NPs, the solution was irradiated with the 808 nm laser (1.0 W cm $^{-2}$) for 5 min and then naturally cooled for 5 min. The switch-on and switch-off transition was repeated 5 times. The photothermal conversion efficiency of HMPB@TK-CCM NPs was calculated based on the method reported by Zuo $et\ al.^{28}$

Fenton performance assessment of HMPB

The catalytic activity of HMPB NPs for peroxidase-like activity was studied using the TMB method. The solutions of HMPB NPs at concentrations of 12, 24, 48, and 96 μg mL⁻¹ were prepared, and an equal volume of water was used as a control. 1 mM H_2O_2 was added to each solution, and the reactions were conducted at room temperature. Subsequently, 100 μ L of TMB (1 mM) was added, and after a 5 min-reaction, the supernatant

was centrifuged and subjected to UV-vis spectroscopy measurement in the range of 550–750 nm. The generation capacity of ${}^{\bullet}$ OH by HMPB NPs was studied using the MB method. The specific steps involved preparing solutions of HMPB at concentrations of 12, 24, 48, and 96 μg mL⁻¹, with an equal volume of water used as a control. 1 mM H₂O₂ was added to each solution, and the reactions were carried out at room temperature. Subsequently, 100 μ L of MB (0.015%) was added, and after a 20 min reaction, the supernatant was centrifuged and subjected to

UV-vis spectroscopy measurement in the range of 550-800 nm.

Drug release performance of HMPB/LAP@TK-CCM

The drug release experiments were divided into four groups: (1) pH 7.4 group, (2) pH 7.4 + laser group, (3) pH 5.0 group, and (4) pH 5.0 + laser group. HMPB/LAP@TK-CCM NP solution (0.1 mg mL⁻¹, 1 mL) was mixed with 1 mL of PBS. For groups (1) and (3) the solution was stored in the dark, while for groups (2) and (4) the solution was irradiated with a 808 nm laser (1.0 W cm⁻²). 0.5 mL of solution was withdrawn and replaced with fresh PBS at the predetermined time. The release profile of LAP was determined by UV-vis absorbance (at 445 nm) according to the calibration curves.

Cell culture

Nanoscale Horizons

After intravenous injection of TK-CM and D-C/M@CM/DiR NPs, in vivo imaging and biological distribution were monitored using an imaging system (IVIS Lumina, USA) at various time points. Subsequently, tumor tissue as well as major organs including the heart, liver, spleen, lungs, kidneys, and others were excised and examined using the same imaging method.

In vivo antitumor effects

Mouse mammary carcinoma cells (4T1) were cultured in RPMI 1640 medium containing 10% fetal bovine serum and 1% penicillin–streptomycin. Mouse embryonic fibroblast cells (3T3) were cultured in DMEM containing 10% fetal bovine serum and 1% penicillin–streptomycin. The cell lines were cultured at 37 $^{\circ}$ C with 5% CO₂.

In vitro homologous targeting study

To detect the *in vitro* homologous targeting ability of HMPB@ TK-CCM NPs, 4T1 and 3T3 cells were added to a confocal dish separately. The old culture medium was replaced with fresh medium containing Cy5 labeled HMPB@TK (HMPB@TK-Cy5), Cy5 labeled HMPB@CCM (HMPB@CCM-Cy5), or Cy5 labeled HMPB@TK-CCM (HMPB@TK-CCM-Cy5); after 4 h of coincubation, the cells were washed three times with PBS, followed by nuclear staining with Hoechst 33342 and membrane staining with cell mask green for 20 min. After staining, the cells were washed three times with PBS to remove excess dye and observed using confocal laser scanning microscopy.

Flow cytometry was used to quantitatively analyze homologous targeting of cells *in vitro*. 4T1 and 3T3 cells were seeded at a density of 1×10^5 cells per well in a 24 well plate. After 24 h of culture, fresh medium containing HMPB@TK-Cy5, HMPB@ CCM-Cy5, or HMPB@TK-CCM-Cy5 was added, and the cells

were co-incubated for another 4 h. The cells were washed three times with PBS and collected. The fluorescence intensity of Cy5 in different cells was detected by flow cytometry.

In vitro cytotoxicity assay

The toxicity of HMPB@TK-CCM, HMPB@TK-CCM + NIR, LAP, HMPB/LAP@TK-CCM, and HMPB/LAP@TK-CCM + NIR on 4T1 cells was determined using the CCK-8 assay. Initially, 4T1 cells were seeded at a density of 1×10^4 cells per well in a 96-well plate and cultured overnight at 37 °C with 5% CO2. Fresh culture medium containing different concentrations of HMPB@ TK-CCM (0, 25, 50, 100, 200 μ g mL⁻¹) and LAP (0, 2.5, 5, 10, 20 μg mL⁻¹) was added and co-incubated with cells for 4 h. Subsequently, the experimental groups requiring laser irradiation were exposed to an 808 nm laser (1.0 W cm⁻², 5 min). The cells were then washed with PBS, and 100 µL of medium containing 10 μL CCK-8 was added. After incubating for approximately 1 h, the absorbance values were detected at 450 nm via a microplate reader. The viability of cells (%) was calculated using (OD_{450sample} - OD_{450background})/(OD_{450control} -OD450_{background}) × 100%. The cytotoxicity of HMPB@TK-CCM on 3T3 cells was determined using the same method.

Live/dead staining assay

4T1 cells were seeded in a 24-well plate at a density of 1 \times 10⁵ cells per well and cultured for 12 h at 37 °C in a 5% CO₂ environment. The cells were treated with various groups: (1) NIR, (2) LAP, (3) HMPB@TK-CCM, (4) HMPB@TK-CCM + NIR, (5) HMPB/LAP@TK-CCM, and (6) HMPB/LAP@TK-CCM + NIR. The concentrations of HMPB and LAP were 5 to 200 μ g mL⁻¹, respectively, and an 808 nm laser with a power of 1.0 W cm⁻² was used. The cells were washed three times with PBS and co-labeled with calcein-AM (green, live cells) and PI (red, dead cells) according to the manufacturer's instructions. Fluorescence microscopy was employed for observation.

Intracellular ROS detection

Cellular ROS levels were detected using the 2,7-dichlorofluorescein diacetate (DCFH-DA) probe. 4T1 cells were seeded in a 24-well plate at a density of 1 \times 10 5 cells per well and cultured overnight. The cells were treated with various groups: PBS, H₂O₂, HMPB/LAP@TK-CCM + H₂O₂, HMPB/LAP@TK-CCM + NIR, and HMPB/LAP@TK-CCM + H₂O₂ + NIR. After different treatments, the cells were washed three times with PBS and stained with DCFH-DA (10 μ M, 1 mL) for 20 min. Finally, observation was conducted using a fluorescence microscope.

Intracellular O2 detection

Intracellular O_2 levels were measured using the $[Ru(dpp)_3]^{2^+}Cl_2$ probe. Initially, 4T1 cells were seeded in cell culture dishes at a density of 1×10^5 cells per dish and cultured overnight in a cell culture incubator. The cells were treated with PBS, H_2O_2 , HMPB/LAP@TK-CCM + H_2O_2 , HMPB/LAP@TK-CCM + NIR, and HMPB/LAP@TK-CCM + H_2O_2 + NIR respectively. Subsequently, $[Ru(dpp)_3]^{2^+}Cl_2$ (10 µg mL⁻¹) was added and incubated

with the cells for 12 h. The cells were then washed three times

with PBS, stained with Hoechst 33342 for 15 min to label the cell nuclei, and finally further washed with PBS to remove excess dye. Cellular observations were performed using confocal laser scanning microscopy (CLSM).

In vivo targeting assessment

Communication

4T1 tumor-bearing mice were intravenously injected with HMPB@TK-DiR or HMPB@TK-CCM-DiR (10 mg kg^{-1} 100 µL). Subsequently, the mice were anesthetized and imaged at different time points via an in vivo imaging system (Perkin-Elmer IVIS Lumina III) with the excitation wavelength at 740 nm and the emission wavelength at 790 nm. For ex vivo fluorescence imaging, mice were sacrificed at 96 h postinjection, and their major organs (hearts, livers, spleens, lungs, and kidneys) and tumor tissues were collected to study the biodistribution of the NPs.

In vivo tumor therapy

SPF-grade female BALB/c mice (4-5 weeks old) were purchased from Beijing Weitonglihua Experimental Animal Technology Co., Ltd. The purchased mice were kept in the Animal Management Center of Jinan University and the animal experiments were approved by the Laboratory Animal Welfare and Ethics Committee of Jinan University (approval number: IACUC-20230616-02). 1×10^6 4T1 cells were subcutaneously injected into the right hind of mice to build the subcutaneous xenograft model. When tumors reached ~ 50 mm³, the 4T1 tumorbearing mice were randomly divided into 5 groups (n = 5): PBS, HMPB/LAP@TK-CCM, HMPB@CCM + NIR, HMPB@TK-CCM + NIR, and HMPB/LAP@TK-CCM + NIR. The group receiving laser treatment was irradiated at the tumor site with an 808 nm laser, delivering a power density of 1.0 W cm⁻² for 5 min, 72 h later as required. The temperature changes were monitored using an infrared thermal imaging camera. Over a 21-day period, the mice's body weight and tumor volume were measured every other day. The formula for calculating tumor volume was $V_{\text{tumor}} = \text{tumor length} \times \text{tumor width}^2/2$, and relative tumor volume was defined as V/V_0 (V: current tumor volume; V_0 : initial tumor volume). Following the completion of treatment, the mice' tumors were dissected for H&E staining, immunofluorescence, and immunohistochemical analysis.

Biosafety assessment

In order to investigate the biosafety of the treatment for mice, blood samples were collected from the mice post-treatment for hematological analysis. Additionally, major organs (hearts, livers, spleens, lungs, and kidneys) were harvested for H&E staining to conduct histological research.

Statistical analysis

The quantitative data analysis was presented as mean \pm standard deviation (SD). Ordinary one-way ANOVA was applied to test the significance of the difference. The p values < 0.05were considered statistically significant (ns, not significant, *p < 0.05, **p < 0.01, ***p < 0.001, ****p < 0.0001).

Conflicts of interest

The authors declare no competing financial interest.

Data availability

The data supporting this article have been included as part of the ESI.†

Acknowledgements

This work was financially supported by the Guangdong Basic and Applied Basic Research Foundation (grant no. 2024A1515 030001) and the National Natural Science Foundation of China (grant no. 51903104). The author gratefully acknowledges the support of the K. C. Wong Education Foundation. The authors thank the Centric Laboratory of Medical College of Jinan University for providing experimental and instrumental platforms.

References

- 1 W. Qiao, J. Chen, H. Zhou, C. Hu, S. Dalangood, H. Li, D. Yang, Y. Yang and J. J. A. S. Gui, A Single-Atom Manganese Nanozyme Mn-N/C Promotes Anti-Tumor Immune Response via Eliciting Type I Interferon Signaling, Adv. Sci., 2024, 11(14), 2305979.
- 2 Y. J. Zhang, P. H. Chen, B. H. Li, H. S. Guo, J. F. Zhu, Z. C. Dang, S. Lei, P. Huang and J. Lin, Comprehensively Optimizing Fenton Reaction Factors for Antitumor Chemodynamic Therapy by Charge-Reversal Theranostics, ACS Nano, 2023, 17(17), 16743-16756.
- 3 W. B. Dirersa, T. C. Kan, G. Getachew, A. Wibrianto, S. Ochirbat, A. Rasal, J. S. Chang and J. Y. Chang, Preclinical Assessment of Enhanced Chemodynamic Therapy by an FeMnO-Based Nanocarrier: Tumor-Microenvironment-Mediated Fenton Reaction and ROS-Induced Chemotherapeutic for Boosted Antitumor Activity, ACS Appl. Mater. Interfaces, 2023, 15(48), 55258-55275.
- 4 R. Xiong, X. Zhu, J. Zhao, G. Ling and P. J. S. M. Zhang, Nanozymes-Mediated Cascade Reaction System for Tumor-Specific Diagnosis and Targeted Therapy, Small Methods, 2024, 2301676.
- 5 L. Y. Wang, M. Gu, X. L. Zhang, T. T. Kong, J. Liao, D. Zhang and J. W. Li, Recent Advances in Nanoenzymes Based Therapies for Glioblastoma: Overcoming Barriers and Enhancing Targeted Treatment, Adv. Sci., 2025, 2413367.
- 6 H. M. Kang, L. M. Chen, Q. Li, H. Chen and L. K. Zhang, Dual-Oxygenation/Dual-FentonSynergistic Photothermal/ Chemodynamic/Starvation Therapy for Tumor Treatment, ACS Appl. Mater. Interfaces, 2023, 15(12), 15129-15139.
- 7 S. S. Ding, L. He, X. W. Bian and G. Tian, Metal-organic frameworks-based nanozymes for combined cancer therapy, Nano Today, 2020, 35, 100920.
- 8 L. Zhang, S. S. Wan, C. X. Li, L. Xu, H. Cheng and X. Z. Zhang, An Adenosine Triphosphate-Responsive Autocatalytic

Fenton Nanoparticle for Tumor Ablation with Self-Supplied HO and Acceleration of Fe(III)/Fe(II) Conversion, Nano Lett., 2018, 18(12), 7609-7618.

Nanoscale Horizons

- 9 Y. Zhou, S. Fan, L. Feng, X. Huang and X. J. A. M. Chen, Manipulating intratumoral Fenton chemistry for enhanced chemodynamic and chemodynamic-synergized multimodal therapy, Adv. Mater., 2021, 33(48), 2104223.
- 10 Y. Hong, Q. Tao, Y.-Y. Liu, Z. Wang, H. Wang and L. J. D. T. Sun, Copper peroxide coated upconversion nanoparticle modified with glucose oxidase for H2O2 selfsupplying starvation-enhanced chemodynamic therapy in vitro, Dalton Trans., 2022, 51(30), 11325-11334.
- 11 S. Li, Q. H. Wang, Z. Jia, M. Da, J. D. Zhao, R. Yang and D. Z. Chen, Recent advances in glucose oxidase-based nanocarriers for tumor targeting therapy, Heliyon, 2023, 9(10), e20407.
- 12 Y. H. Fu, J. L. Sun, Y. H. Wang and W. A. Li, Glucose oxidase and metal catalysts combined tumor synergistic therapy: mechanism, advance and nanodelivery system, J. Nanobiotechnol., 2023, 21(1), 400.
- 13 W. Jiang, X. Guan, W. Liu, Y. Li, H. Jiang and T. Ngai, Pickering emulsion templated proteinaceous microparticles as glutathione-responsive carriers for endocytosis in tumor cells, Nanoscale Horiz., 2024, 9(4), 536-543.
- 14 X. Dai, Y. Q. Zhu, M. Su, J. B. Chen, S. Shen, C. F. Xu and X. Z. Yang, Rigid Shell Decorated Nanodevice with Fe/HO Supply and Glutathione Depletion Capabilities for Potentiated Ferroptosis and Synergized Immunotherapy, Adv. Funct. Mater., 2023, 33(27), 2215022.
- 15 X. Gong, J. Wang, L. Yang, L. Li, X. Gao, X. Sun, J. Bai, J. Liu, X. Pu and Y. J. S. Wang, Enhanced Chemodynamic Therapy Mediated by a Tumor-Specific Catalyst in Synergy with Mitophagy Inhibition Improves the Efficacy for Endometrial Cancer, Small, 2023, 19(33), 2301497.
- 16 C. Liu, N. Yang, M. Li, S. Song, W. Zhou, J. Ren, W. Han, Y. Li and C. J. M. C. F. Yu, Palladium-based metal-organic coordination nanoparticles for efficient tumor treatment via synergistic enhancement of ROS production, Mater. Chem. Front., 2024, 8(18), 3028-3036.
- 17 L. Dai, X. Li, X. Duan, M. Li, P. Niu, H. Xu, K. Cai and H. J. A. S. Yang, A pH/ROS cascade-responsive chargereversal nanosystem with self-amplified drug release for synergistic oxidation-chemotherapy, Adv. Sci., 2019, 6(4), 1801807.
- 18 L. He, G. Ding, S. S. You, S. Lu, X. F. Huang, L. Li and X. L. Yu, Construction of Cu/ZIF-67/Prussian Blue Nanostructures with Photothermal-Enhanced Multizyme Activity for Cancer Therapy, ACS Appl. Nano Mater., 2023, 6(12), 10779-10790.
- 19 H. Wu, L. Xie, W. P. Shi, T. Y. Zhou, T. B. Yu and Y. Z. Zhang, Iridium-Doped Prussian Blue Nanozymes for Photothermal and Photodynamic Therapy, ACS Appl. Nano Mater., 2024, 7(16), 19130-19142.
- 20 N. Chakraborty, I. Roy, P. Kumar, S. Singh, R. Pathak, V. Gautam and H. K. Gautam, Nanoscale Prussian Blue and Its Analogues: Design and Applications in Infection

- Control, Wound Healing and Beyond, Pharmaceutics, 2024, **16**(12), 1616.
- 21 D. D. Wang, J. W. Liu, C. L. Wang, W. Y. Zhang, G. B. Yang, Y. Chen, X. D. Zhang, Y. L. Wu, L. Gu, H. Z. Chen, W. Yuan, X. K. Chen, G. F. Liu, B. Gao, Q. W. Chen and Y. L. Zhao, Microbial synthesis of Prussian blue for potentiating checkpoint blockade immunotherapy, Nat. Commun., 2023, 14(1), 2943.
- 22 W. Wu, L. Yu, Y. Pu, H. Yao, Y. Chen and J. J. A. M. Shi, Copper-enriched prussian blue nanomedicine for in situ disulfiram toxification and photothermal antitumor amplification, Adv. Mater., 2020, 32(17), 2000542.
- 23 H. Han, S. Wang, M.-A. Shahbazi, I. S. Zuhorn, Z. Cai, J. Chen, J. Li, Y. Chen, Y. Du and R. Bártolo, Reactive oxygen species switcher via MnO2-coated Prussian blue loaded hyaluronic acid methacrylate hydrogel microspheres for local anti-tumor treatment, J. Controlled Release, 2025, 378, 350-364.
- 24 J. L. Yao, J. Xing, Y. X. Yao, X. X. Wu, Y. Qiu, Z. H. Li, S. Y. Xiong, H. Peng, F. Yang and A. G. Wu, Ytterbium Doping-Retooled Prussian Blue for Tumor Metabolism Interference Therapy, ACS Nano, 2024, 18(52), 35758-35770.
- 25 Y. T. Hao, L. Z. Mao, R. J. Zhang, X. S. Liao, M. M. Yuan and W. Z. Liao, Multifunctional Biodegradable Prussian Blue Analogue for Synergetic Photothermal/Photodynamic/Chemodynamic Therapy and Intrinsic Tumor Metastasis Inhibition, ACS Appl. Bio Mater., 2021, 4(9), 7081-7093.
- 26 B. R. Oi, Z. Xiao, J. Huang, G. Z. Zhou, T. Zhou, G. Y. Liu and Z. Li, Photothermal and ROS-mediated cellular apoptosis using copper-driven Prussian blue analog nanoparticles with bimetallic reaction centres, Chem. Eng. J., 2024, 498, 155432.
- 27 X. L. Liu, X. Zhong and C. Li, Challenges in cell membranecamouflaged drug delivery systems: Development strategies and future prospects, Chin. Chem. Lett., 2021, 32(8), 2347-2358.
- 28 Y. C. Zuo, C. M. Huo, Y. Chen, P. L. Ding, S. Y. Tong, W. Xue and J. Y. J. A. H. M. Zhu, Cancer-Thylakoid Hybrid Membrane Camouflaged Thulium Oxide Nanoparticles with Oxygen Self-Supply Capability for Tumor-Homing Phototherapy, Adv. Healthcare Mater., 2024, 13(11), 2303779.
- J. Y. Zhu, C. Sevencan, M. K. Zhang, R. S. A. McCoy, X. G. Ding, J. J. Ye, J. P. Xie, K. Ariga, J. Feng, B. H. Bay and D. T. Leong, Increasing the Potential Interacting Area of Nanomedicine Enhances Its Homotypic Cancer Targeting Efficacy, ACS Nano, 2020, 14(3), 3259-3271.
- J. Y. Zhu, D. W. Zheng, M. K. Zhang, W. Y. Yu, W. X. Qiu, J. J. Hu, J. Feng and X. Z. Zhang, Preferential Cancer Cell Self-Recognition and Tumor Self-Targeting by Coating Nanoparticles with Homotypic Cancer Cell Membranes, Nano Lett., 2016, 16(9), 5895-5901.
- 31 Y. Cheng, R. Zheng, X. Wu, K. Xu, P. Song, Y. Wang, J. Yan, R. Chen, X. Li and H. J. A. H. M. Zhang, Thylakoid Membranes with Unique Photosystems Used to Simultaneously Produce Self-Supplying Oxygen and Singlet Oxygen for Hypoxic Tumor Therapy, Adv. Healthcare Mater., 2021, 10(6), 2001666.

32 S. K. Shen, Y. Y. Wang, J. X. Dong, R. Zhang, A. Parikh, J. G. Chen and D. D. Hu, Mimicking Thylakoid Membrane with Chlorophyll/TiO/Lipid Co-Assembly for Light-Harvesting and Oxygen Releasing, ACS Appl. Mater. Interfaces, 2021, 13(9), 11461-11469.

Communication

- 33 X. R. Chen, B. B. Liu, R. L. Tong, L. Zhan, X. L. Yin, X. Luo, Y. N. Huang, J. F. Zhang, W. He and Y. L. Wang, Orchestration of biomimetic membrane coating and nanotherapeutics in
- personalized anticancer therapy, Biomater. Sci., 2021, 9(3), 590-625.
- 34 K. Y. Wang, B. Yang, H. Ye, X. B. Zhang, H. Song, X. Wang, N. Li, L. Wei, Y. Wang, H. T. Zhang, Q. M. Kan, Z. G. He, D. Wang and J. Sun, Self-Strengthened Oxidation-Responsive Bioactivating Prodrug Nanosystem with Sequential and Synergistically Facilitated Drug Release for Treatment of Breast Cancer, ACS Appl. Mater. Interfaces, 2019, 11(21), 18914-18922.